Wavelet-Based Image Reconstruction for Hard-Field Tomography With Severely Limited Data

Wavelet-Based Image Reconstruction for Hard-Field Tomography with Severely Limited Data

N.Terzija, *Member, IEEE*, H.McCann, *Senior Member, IEEE*

Abstract— **We introduce a new wavelet-based hard-field image reconstruction method that is well suited for data inversion of limited path-integral data obtained from a geometrically sparse sensor array. It is applied to a chemical species tomography system based on near-IR spectroscopic absorption measurements along an irregular array of only 27 paths. This system can be classified as producing severely limited data, where both the number of viewing angles and the number of measurements are small. As shown in our previous work, the Landweber iteration method allows stable solution of this tomography problem by incorporating suitable *a priori* information. In the new method, a 2-D discrete wavelet transform has been used as a smoothing function. We present a method of designing the optimal wavelet-based smoothing function, depending on *a priori* knowledge of the subject. The significance of the particular wavelet filter selected is considered in terms of the accuracy of reconstruction of the spatial location and shape of the gas distribution. Results are presented for simulated phantoms using different sensor arrays and for experiments with propane plumes, showing excellent spatial localization and quantification. The computational time of the iterative algorithm is significantly reduced by applying the wavelet transform method. Some of our conclusions are applicable to other hard-field tomographic modalities in applications where similar constraints may be encountered.**

***Index Terms*— Tomography, image reconstruction, wavelet transform, limited data**

I. Introduction

IMAGE reconstruction from limited data is a complex problem of wide interest in the field of industrial process tomography. In process engineering applications of tomography, it is common to have very limited measurement access for sensor installation and to encounter hostile environments that are rapidly changing. The use of X- and gamma-ray CT has been developed by Munshi and co-workers [1] to reconstruct images of liquid/gas multi-phase flow using attenuation measurements along a small number of beams forming only one projection through the subject. Wright *et al.* [2,3] present a further example, using a chemically selective optical tomography system based on the principle of spectroscopic absorption, for high-speed imaging of hydrocarbon fuel vapour within one cylinder of a multi-cylinder internal combustion engine. The latter application places very severe constraints on both the number and positioning of measurement paths (beams) through the subject, resulting in an irregular and sparse sensor array with 27 beams which is characteristic of the application. This system can be regarded as belonging to a category of systems with severely limited data, in which both the number of viewing angles and the number of measurements are small. Any image reconstruction approach chosen for this application must address these issues.

One of the most important tools used in limited data reconstruction is *a priori* information about the subject, which may concern the smoothness of the subject, knowledge of its non-negativity, the image boundary, or knowledge of the expected value in some parts of the subject. Some authors have investigated image reconstruction algorithms that can be modified in order to incorporate all available *a priori* information. In particular, iterative algebraic reconstruction techniques [4], [5] have been found to be very successful. The use of transform-based inversion techniques [6], [7] is only applicable to sensor and beam arrangements described by projections arranged at regularly spaced viewing angles, with each projection comprising many beams. Besides these techniques, there are other image reconstruction concepts which can be used only in cases where the distribution of the concentration field is known to some extent (e.g. the Smooth Basis Function Minimization (SBFM) technique [8]).

Methods of image reconstruction based on the Wavelet Transform (WT) have not been widely used in tomography, although wavelets have been used to improve the characteristics of the sensors [9], [10]. However, three main categories of wavelet approaches for image reconstruction have been identified. The first wavelet approach [11]-[15] is used primarily in medical applications and is based on the combination of the Radon and wavelet transforms by incorporating wavelet filtering into filtered back-projection, in order to achieve a "near-local" representation of the global Radon transform. The emphasis of this approach is on reducing the patient's exposure to X-rays by constructing a

N. Terzija and H. McCann are with The University of Manchester, Manchester, United Kingdom, (e-mail: natasa.terzija@manchester.ac.uk, h.mccann@manchester.ac.uk).

"region of interest" that requires fewer X-ray projections to be taken. However, in most industrial applications, limitations of speed, accessibility, and/or cost, may reduce the number of measurements and projection angles and consequently, the quality of data. Therefore, this wavelet approach is not particularly useful in industrial applications, since there is little motivation to reduce dose levels, and because of the limited data problem. The second category of wavelet approach applies wavelets for image de-noising and feature extraction. The wavelet transform is applied to the projections in order to isolate features of interest (such as edges) and reconstruct the images only from those features [16], [17]. The third category identified is a regularisation approach, called the Wavelet-Vaguelette decomposition [18], which is a wavelet analogue of the singular value decomposition. This method is used as a framework from which expressions for the necessary wavelet coefficients are derived, and then the wavelet shrinkage is applied to the wavelet coefficients to regularize the solution [19], [20]. Other researchers [21], [22] have used wavelet transforms as a form of regularisation to improve the performance of the well-known non-iterative Filtered Back Projection.

To the best of our knowledge, 2D wavelet methods in general have not been proposed for use with *severely limited data*; due to lack of space for sensor installation, or incompatible environmental issues, most industrial process tomography systems, in fact, produce severely limited data. Several wavelet-based regularisation algorithms [23], [24] were proposed for the problem of limited-angle tomography, where the wavelet transform is used to incorporate *a priori* information of the subject. Although these algorithms show encouraging performance, they have been studied mostly in cases where only a small angular range of projections is missing and therefore, it is not possible to conclude whether these can be applied in the case of severely limited data.

In this paper a new image reconstruction method will be described; it is based on the 2-dimensional wavelet transform, and it has several potential advantages for severely limited data problems when compared to conventional methods. The wavelet transform provides a set of coefficients representing the localized information in a number of frequency bands. If certain wavelet coefficients related to the high-frequency information are not included in the inverse wavelet reconstruction process, the reconstructed image shows smoothing effects. Moreover, the selection of the wavelet filter can be optimized in the knowledge of the beam arrangement, which is potentially of great utility for sparse and irregular measurement geometries, and offers scope to improve the design of the sensor array. To the best of our knowledge, this paper is the first to apply the wavelet transform to tomographic reconstruction in the spatial domain. As noted above, selection of the wavelet filter is strictly application-dependent. One objective of this paper is to investigate if image reconstruction accuracy is influenced by the particular wavelet filter chosen. The performance of the method is tested on both simulated and experimental data.

The paper is organised as follows: In Section 2 the image reconstruction method is presented, along with a description of important wavelet concepts. Section 3 gives the results of investigation and method testing on both regular and irregular, sparse arrays of beams due to limited sensor access. Sections 4 and 5 give discussion and conclusions.

II. IMAGE RECONSTRUCTION METHOD

In our previous work [25] it is shown that the Landweber iteration method, which offers the ability to be modified in order to take into account additional regularization, allows stable solution of the tomography problem in a system with an irregular sensor and beam array and with a severely limited number of measurements. The main purpose of regularization is to filter out noise and to make the solution smoother. The regularization can also include *a priori* information about the true solution which facilitates the minimization process to converge as close as possible to the true solution. For example, value constraints, such as a non-negativity constraint, can be applied to the solution as the lower concentration limit in order to maintain physically meaningful concentrations. The smoothing process filters out the high-frequency components, thereby giving a smooth final solution. The high-frequency components filtered out by the regularization technique relate to edges and discontinuities. Therefore, the smoothing function should be carefully selected since the high-frequency components may contain significant information about the solution (e.g. about the boundaries). In order to satisfy those requirements we propose a wavelet-based smoothing function, which is described below.

A. Wavelet analysis

The wavelet transform has the key feature of spatial localization of frequency content of signals and images and has found application in a number of signal and image processing applications [26]. Although the theoretical foundations of the WT do not constitute the main topic of the present study, it is helpful to introduce those basic concepts of the WT which are significant for the proposed methodology. In general, WT provides a local representation of the spectral properties of an image and it enables work at different levels of spatial resolution, operating as a tool for *multiresolution analysis*. Multiresolution analysis allows retrieval of layers of details which have different spatial sizes. This is achieved by separating the spatial frequencies contained in the image. This multiresolution approach [27] is commonly achieved by using an algorithm that permits compression of data by decimating the image.

The WT decomposes a signal into a family of wavelet functions, which are dilations and translations of a single prototype wavelet function, called the *mother wavelet*. There are many algorithms available to perform the Discrete wavelet

transform (DWT) of an image. A widely used approach is the *pyramidal methodology* which consists of reducing the size of the image iteratively to obtain progressively smoother and smoother versions of the initial image.

Starting from the original signal $f(n)$, the recursive formula for the wavelet decomposition is given by:

$$f_j(n) = \sum_k h(2n-k) f_{j-1}(k) \quad (1)$$

$$W_{2^j}(f(n)) = \sum_k g(2n-k) f_{j-1}(k) \quad (2)$$

where for a fixed decomposition level j, $\forall j > 0$, $W_{2^j}(f(n))$ is called the differential (or detail) signal and $f_j(n)$ is called the averaged (or approximation) signal. The sequences $h(n)$ and $g(n)$ are called the scaling function and the wavelet, respectively, and satisfy $g(n) = (-1)^n h(1-n)$. The scaling function $h(n)$ is usually a low-pass filter, and the wavelet $g(n)$ is a high-pass filter. At each level *j,* the approximation signal from the previous level is convolved with the low-pass filter $h(n)$ and high-pass filter $g(n)$, and downsampled by a factor two. The reconstruction of the signal from its wavelet coefficients at all levels of approximation and detail, is simply

$$f_{j-1}(n) = \sum_k h(2k-n) f_j(k) + g(2k-n) W_{2^j} \quad (3)$$

The simplest way to compute the two-dimensional (2-D) DWT is to apply one-dimensional (1-D) DWT over image rows and columns separately, as illustrated schematically in Fig. 1. Thus, the image decomposition is obtained with separable filtering along the abscissa and ordinate, using the same algorithm as in the 1-D case. This transform decomposes images by an overall scale factor four, providing at each level one low-resolution approximation subband and three detail subbands. The resulting four subbands represent all possible combinations of high- and lowpass filtering in two directions. For each resolution, there are three types of detail: horizontal (HL), vertical (LH) and diagonal (HH).

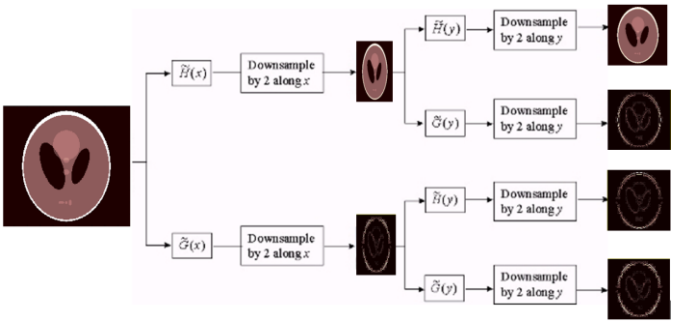

Fig. 1: 2-D Discrete wavelet transform.

For an image $f(n,m)$, the 2D wavelet transform at decomposition level *j* is defined recursively as:

$$f_j(n,m) = \sum_{k_1}\sum_{k_2} h(2n-k_1)h(2m-k_2) f_{j-1}(k_1 k_2) \quad (4)$$

$$W_{2^j}^{HL}(f(n,m)) = \sum_{k_1}\sum_{k_2} g^{HL}(2n-k_1, 2m-k_2) f_{j-1}(k_1,k_2)$$

$$W_{2^j}^{LH}(f(n,m)) = \sum_{k_1}\sum_{k_2} g^{LH}(2n-k_1, 2m-k_2) f_{j-1}(k_1,k_2)$$

$$W_{2^j}^{HH}(f(n,m)) = \sum_{k_1}\sum_{k_2} g^{HH}(2n-k_1, 2m-k_2) f_{j-1}(k_1,k_2) \quad (5)$$

where $g^{HL}(n,m) = g(m)h(n)$, $g^{LH}(n,m) = g(n)h(m)$ and $g^{HH}(n,m) = g(n)g(m)$. The original image $f(n,m)$ can be recovered using a recursive formula analogous to Equation (3).

The 2-D DWT was defined above as a filtering process which produces at each level j of decomposition an approximation subband which represents a smoother version of the initial image. If we apply the inverse DWT only to the approximation subband, by setting to zero the detail coefficients $W_{2^j}^{HL}(f(n,m))$, $W_{2^j}^{LH}(f(n,m))$, $W_{2^j}^{HH}(f(n,m))$, given in equation (5), we will get a smooth image with the same size as the initial image. Since a large number of wavelet filters are available, it is difficult to select an optimal mother wavelet for a specific application. We illustrate the issue here with an example that shows the differences between the smoothed images which are obtained by applying to a standard phantom three different types of mother wavelet filter, Haar, Daub 8 and Daub 11 [28], which have different abilities to filter out high frequency components, i.e. to preserve different shapes. The smoothed images, shown in Fig. 2, are obtained by applying the inverse DWT only to approximation subband $f_j(n,m)$ for *j*=1, 2 and 3.

Daubechies wavelet filters [28], in particular those filters with higher orders, which are widely used in image analysis applications, show very good performance in preserving the approximation information stored in the original signals. This can be seen in Fig. 2 (middle and bottom rows), where the round shape was clearly preserved even at the third level of approximation. Wavelet smoothing in general introduces changes in magnitude which can be seen from comparison of the colour scales in Fig. 2.

From the above examples we can conclude that wavelet smoothing requires the multi-level decomposition to be customized by specifying the number of decompositions, the type of the mother wavelet filter and the percentage of detail coefficients to be cut out.

B. Wavelet function assessment and selection

In this paper we propose a wavelet smoothing function which is particularly suitable for hard-field tomographic image reconstruction iterative algorithms that operate in the spatial domain. Any simple linear projection iterative technique

contains artefacts in its early iterations, i.e. the beam paths, and information on the subject distribution (see Fig. 3(b)). The next step in these algorithms should ideally filter out those artefacts, providing the smoothness of the subject distribution at the same time. In order to achieve that, we apply the DWT to decompose the image into the approximation and detail with the aim of representing the subject distribution by the approximation subband; the artefacts, which in this case have clear line shapes, are represented by the detail subbands. The smoothed image representing the true distribution of the measured subject is then obtained by applying the inverse DWT only to the approximation subband $f_j(n,m)$.

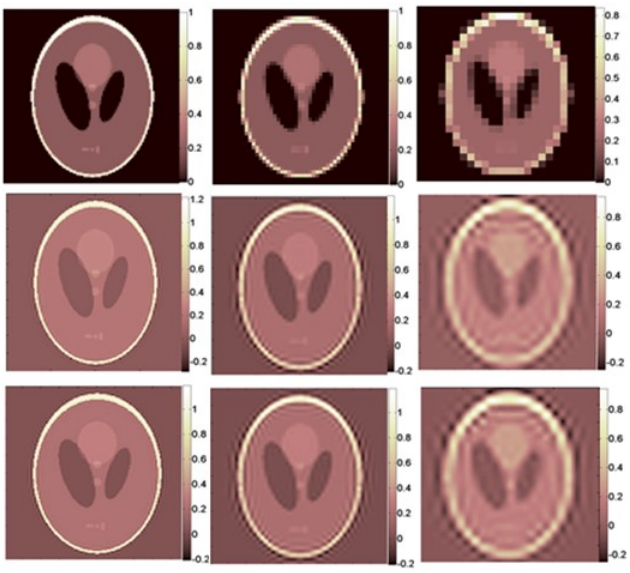

j=1 *j*=2 *j*=3

Fig. 2: Wavelet-smoothed images of the Shepp-Logan 11 phantom, obtained by applying the inverse DWT to approximation subband $f_j(n,m)$ for *j*=1, 2 and 3, using 3 different mother wavelets: Haar, Daub 8 and Daub 11, in top, middle and bottom rows, respectively.

In Fig. 2 it is shown that the level of wavelet decomposition has a significant influence on the quality of the wavelet smoothing; when j increases, we have a reduction in high frequency content. It is important, therefore, to limit the level of decomposition. We concluded that three levels of decomposition were adequate because the subject distribution was fully represented at the appropriate degree of spatial resolution by the approximation subband of the third level and the artefacts were located in the details of all three levels of the decomposition. Furthermore, Daubechies wavelet filters, which are similar in effect to weighted averaging, were selected to be used in our method. Fig. 3 (c) shows 3-level DWT decomposition with a Daubechies wavelet filter. Fig. 3(d) presents the image reconstruction result after the first Landweber iteration using wavelet smoothing, i.e. wavelet reconstruction only from the approximation subband $f_j(n,m)$ for *j*=3. It can be observed that the DWT applied in this way is able to localize the distribution of the subject immediately after the first iteration and to filter out the artefacts. Furthermore, additional enhancement of that image can be performed simply by further selection of the coefficients of the approximation subband. The coefficients with small magnitude in the approximation subband mostly correspond to the flat image region while those with higher magnitude effectively represent the image discontinuities. However, those discontinuities are actually represented with a very small number of wavelet coefficients. There are many ways to perform the selection of the wavelet coefficients. We investigated 3 types of coefficient selection, discarding the coefficients which are smaller than a threshold chosen to be a percentage of the largest coefficient in the approximation subband. Type 1 thesholding consists of discarding all coefficients which are smaller than the (positive-valued) threshold; type2 is a conventional hard threshold; type3 is a conventional soft threshold. To evaluate the effects of thesholding on image quality, we calculated, for each type of coefficient selection, the average image error per pixel:

$$avv\_err = \frac{\sum_{x,y} |f(x,y) - h(x,y)|}{MxN} \qquad (6)$$

where f and h are the reference and reconstructed images, respectively, with dimensions $M \times N$. For the case simulated in Fig. 3(a), the average error as a function of threshold value is shown in Fig. 4, for each type of thresholding, after the Landweber iteration procedure reaches convergence Even when retaining only a small percentage of approximation coefficients we can obtain good visual quality for both type3 and type1 thresholding. Clearly, many theshold values are possible, but equally clearly, type 1 thesholding provides the most stable solution.

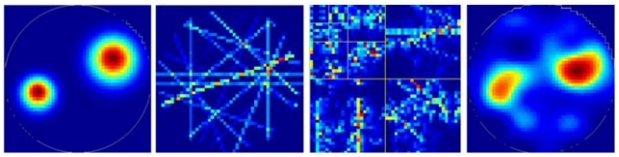

(a) (b) (c) (d)

Fig. 3: (a) Simulated phantom distribution; (b) reconstructed image solution after first Landweber iteration; (c) 3-level DWT decomposition of the solution in (b) with Daubechies 10 wavelet; (d) inverse DWT applied only to the approximation subband of the third decomposition level.

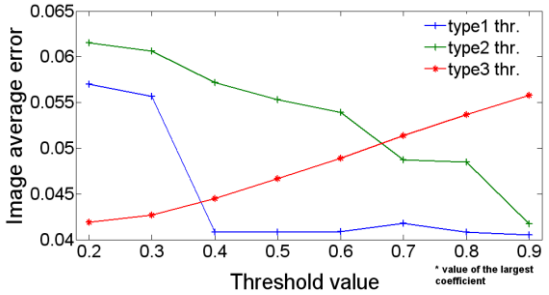

Fig. 4: Effects of different types of thresholding of approximation coefficients on image quality, expressed in the form of average image error.

C. Image reconstruction algorithm

The wavelet-based iterative Landweber algorithm is performed in the following steps:

1. Calculate an initial estimate $\mathbf{g}_1$ by solving the inverse problem as:

$$\mathbf{g}_1 = \mathbf{S}^T \mathbf{v} \tag{7}$$

where $\mathbf{g}_1$ is the estimate of concentration distribution vector $\mathbf{c}$ in each of N pixels in the imaging space, $\mathbf{v}$ is the measurement vector of L, the sensitivity matrix $\mathbf{S}$ is defined from $\mathbf{v} = \mathbf{S}\mathbf{c}$, and $\mathbf{S}^{\mathrm{T}}$ is its N x L transpose which is here used as an approximation to $\mathbf{S}^{-1}$, and

2. Iteratively calculate the solution $\mathbf{g}$ in the image space by:

$$\mathbf{g}_{k+1} = \mathbf{g}_k + \alpha \mathbf{S}^{\mathrm{T}} \left(\mathbf{v} - \mathbf{S}\mathbf{g}_k \right) \tag{8}$$

where k is the iterative step number and α is the relaxation parameter.

3. Set to zero any negative elements of $\mathbf{g}_{k+1}$.

4. Apply the wavelet smoothing to $\mathbf{g}_{k+1}$ by decomposing the solution into 3 levels of DWT using the Daubechies orthogonal wavelet filters Additionally, choose the threshold value and perform the chosen type of thresholding, keeping the rest of the coefficients unchanged. Next, apply the inverse DWT on the approximation subband only.

5. Repeat steps 2 to 5 or stop the iteration process if the defined stopping criterion is satisfied.

Iterative techniques widely use the residual $\left(\mathbf{v} - \mathbf{S}\mathbf{g}_k \right)$ to define a stopping criterion. When the current approximation of the solution $\mathbf{g}_k$ is not close to the true solution, the residual is quite large and the data error is negligible as compared to the size of the residual. As the iteration process continues, the value of the residual decreases while the data error contribution gradually increases. To stop the iteration process, we use the mean normalized difference e between the current and previous solutions, calculated by:

$$e = \left\| \mathbf{g}_{k+1} - \mathbf{g}_k \right\| / \left\| \mathbf{g}_k \right\| \tag{9}$$

When e is less than a predetermined threshold, the procedure is stopped.

Suitable selection of the relaxation parameter α in equation (8) continues to be a matter of great interest in tomography research. Large values of α lead to rapid convergence but increase the risk of instability. Conversely, small values of α provide slow, but reliable convergence. An upper limit for α can generally be determined by using the following expression [29]:

$$0 < \alpha < s\left(\left\| \mathbf{S}^T \mathbf{S} \right\|_2 \right)^{-1} \tag{10}$$

in which the bracketed term is the reciprocal of the Euclidean matrix norm. .

III. Performance Testing and Results

The objectives of this section are to investigate whether the particular wavelet filter selected plays an important role in reconstructing accurately the spatial localization and shape of the gas distribution, and its influence on the computation time of the algorithm. The method was tested on two different sparse sensor array geometries: an irregularly arranged set of beams, described in [3], [25], and an example of a regular beam array with a limited number of angles, similar to that in [2]. Various simulated phantoms and real experimental data were used to test the performance of the reconstruction method and to investigate the effect of varying the reconstruction input parameters. Initially, simulations were run using many wavelet families (e.g. Daubechies, Haar, XXX, YYY and ZZZ), that were considered to be reasonable candidates for the present application. Only the Daubechies familiy gave useful results, in terms of reproducing the known distribution. We investigated various Daubechies wavelet filters and concluded that only four of them give reasonable results. Therefore, we present here the image reconstruction results with wavelet smoothing using Daub8, Daub9, Daub10 and Daub11 wavelet filters.

A. Irregular sensor array geometry

Figure 5(a) shows the 27-beam measurement geometry used to test the performance of the new algorithm; the small number of hard-field measurements, arranged at irregular angles, gives sparse data. The geometry was designed for the multi-cylinder engine application [3] and determined by physical constraints on sensor installation such as the physical size of the collimators and the available regions of the cylinder wall. Figure 5(b) shows the corresponding circular discretized imaging space as a subset of a 50 x 50 Cartesian grid. The beams in our measurement system are less than 1mm wide.

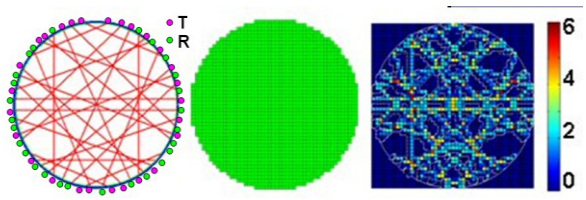

Fig. 5: Irregular and limited-data measurement geometry: (a) irregular 27-beam arrangement (b) image solution space; (c) sensitivity map.

Each pixel in the discretized imaging space may contribute to

the measurements made by one or more beams, providing both angular and spatial information about the subject that is greater for those pixels which are crossed by several beams rather than a single beam. However, the overall sensitivity of the measurement system is very sparse, having only a few pixels that are crossed by two or more beams. The majority of the pixels have no sensitivity in that they are not intersected by any beam. This sparse sensitivity is illustrated in figure 5(c). Therefore the limited and uneven spatial information from such a measurement system can only be exploited by using *a priori* information to estimate the overall subject distribution. Therefore, smoothing (in the present case, using the 2D wavelet transform) is used as *a priori* information to remove the artefacts resulting from the narrow beam paths (see Figure 3(b)) and those arising from poor coverage of the sensor array in the Radon space.

Firstly, we selected the parameters of the Landweber iteration process which include the relaxation parameter α and the stopping criterion. Considering equation (10) and the sensitivity map used for our measurement system, we found that consistent results were obtained by setting α to 0.01. Also the best imaging results were obtained for the threshold value e set to 4%.

The image reconstruction results obtained from simulations consisting of single- and double-plume inhomogeneities are presented in Figs. 6-8. We performed the image reconstruction algorithm using two types of thesholding, type 1 and type 3, and investigated the effects of various threshold values on the image quality. The thresholds are varied in the range from 20% to 90% of the value of the largest coefficient in the approximation subband. For each filter and type of thesholding we calculated the average image error. Table 1 shows, for each case, the minimum average error value obtained. The results clearly show that type 1 thesholding produces better results in all cases but the threshold value varies in the range from 20 to 40% of the largest coefficient. In the case of type 3 thesholding the best results are obtained with a threshold value of 20% of the largest coefficient.

Fig. 6 shows the image reconstruction results from a simulated phantom consisting of a single soft-edged plume, defined by a cosine function for two types of thesholding: Fig 6(a) for type 1 and Fig. 6(b) for type 3 thesholding. The reconstructions from phantoms with two soft-edged plumes, described by a Gaussian function, are presented in Figs. 7 and 8. The concentration content in all figures is given by the colour bar shown, and the colours are globally scaled. The number of iterations needed to satisfy the stopping criterion in the Landweber iteration process is also given in each figure. . In all cases, only a very low number of iterations is needed, which significantly improves the computation time of the algorithm. In terms of the fidelity of the reconstructed image to the simulated phantom, Table 1 shows there are some variations in performance between the filters. It can be seen from these figures, that the reconstructions represent well the approximate size and locality of the simulated plumes. In the case of two plumes with different absorptions, presented in Fig. 7, good sensitivity to variation of concentration is evident. From the colorbars in Figs. 6-8 consistent imaging of the concentration is evident in all image reconstructions from simulated data.

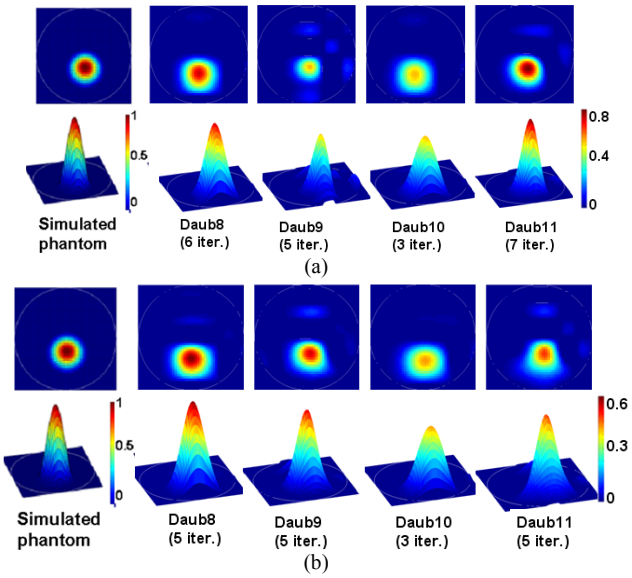

Fig. 6: Image reconstructions obtained from simulated noise-free data using Daub8, Daub9, Daub10 and Daub11 (a) using type 1 thresholding , (b) using type 3 thresholding..

.

Furthermore, we tested our algorithm using real data obtained from experiments with various diameters of propane plume, either singly or in pairs [25], using the value 77.7 $Lmol^{-1}m^{-1}$ for the propane absorption coefficient at 1700nm. Available nozzle configurations included diameters D/3, D/4, D/5 and combinations, where the sensing field diameter, D, was 89 mm. Although the sensor system used in this study featured 27 optical beams, only 26 were operational during these experiments.

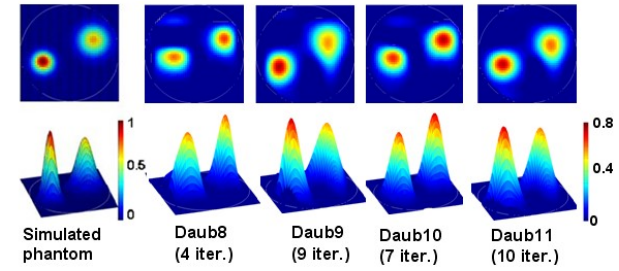

Fig. 7: Image reconstructions obtained from simulated noise-free data using Daub8, Daub9, Daub10 and Daub11.

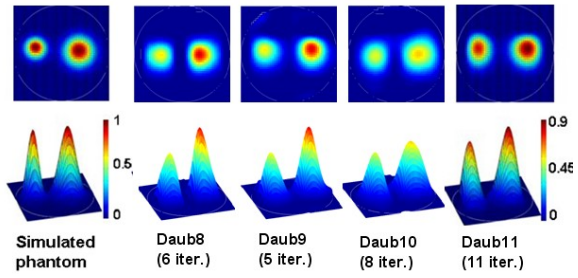

Fig. 8: Image reconstructions obtained from simulated noise-free data using Daub8, Daub9, Daub10 and Daub11.

Table 1: Results of reconstruction using different wavelet smoothing and two types of thresholding..

		daub8	daub9	daub10	daub11
fig.6	type1 thr	0.0227	0.031	0.028	0.0213
	coef.	0.3	0.4	0.4	0.3
	type3 thr	0.0273	0.0295	0.0307	0.0277
	coef.	0.2	0.2	0.2	0.2
fig7	type1 thr	0.0412	0.0396	0.035	0.0429
	coef.	0.4	0.2	0.2	0.2
	type3 thr	0.0451	0.0487	0.0443	0.0518
	coef.	0.2	0.2	0.2	0.2
fig.8	type1 thr	0.0389	0.0375	0.0419	0.0353
	coef.	0.4	0.4	04	0.3
	type3 thr	0.0407	0.0373	0.0432	0.0371
	coef.	0.2	0.2	0.2	0.2

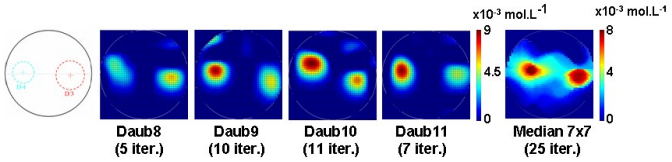

Fig. 9: Image reconstructions obtained from experimental measurements on the phantom shown in the leftmost diagram, using the Landweber technique with smoothing by Daub8, Daub9 , Daub10, Daub11, and a median filter.

Fig. 9 shows the quantitative reconstructions derived from measurements of an asymmetric double plume phantom (one D/4 and one D/3 plume, positioned D/4 apart). The globally scaled reconstructions in fig. 9 use 4 different Daubechies' wavelet filters. Very similar results were obtained with odd-length Daubechies wavelet filters, and the Daub 11 filter showed slightly better performance. All the images produced with the Daubechies filters show much better separation of the two plumes compared with the image produced by the median 7x7 filter, as well as a general reduction of artefacts. Quantitative image reconstruction results for a D/5 propane plume in five different positions are given in Fig. 10 using the Daub 11 filter, with all reconstructions globally scaled. Successful localization of the single plume is evident in each case, with sharper reproduction of the plume than is achieved using the median 7x7 filter (figure 11).

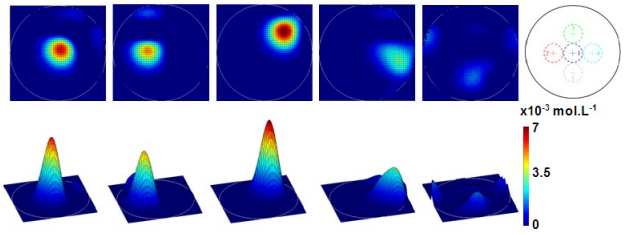

Fig. 10: Image reconstructions obtained from experimental measurements on the phantom shown in the rightmost diagram (D/5 in 5 positions) using Daub11, after 12, 9, 8, 9, 8 iterations, respectively.

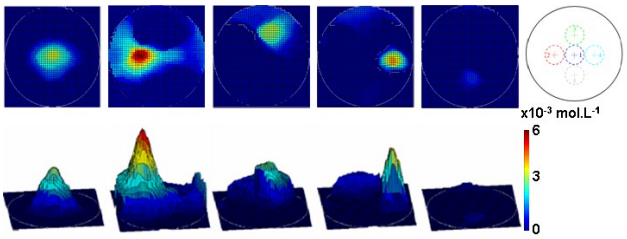

Fig. 11: Image reconstructions obtained from experimental measurements on the phantom shown in the rightmost diagram (D/5 in 5 positions) using the median 7x7 filter, after 25 iterations.

B. Regular sensor array geometry

The regular geometry used to test the performance of our algorithm is shown in Fig. 12(a), and consists of four parallel-beam projections positioned at four different angles (0◦, 45◦, 90◦ and −45◦), each containing 8 beams; this is similar to the array used in [2]. The sensitivity map, calculated in the same way as in the irregular case, is presented in Fig. 12(b), and the same parameters were used for the Landweber algorithm.

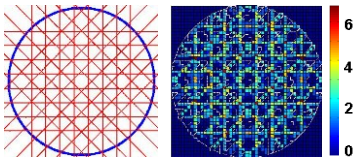

(a) (b)

Fig. 12: Regular and limited-data measurement geometry: (a) Regular 32-beam arrangement (b) sensitivity map.

Simulations consisted of two double-plume and one triple-plume phantoms with soft edges, defined by a cosine function. Image reconstructions of the two double-plume phantoms, using all 4 preferred Daubechies' filters, are shown in Fig. 13. Fig. 14(a) shows reconstructions of triple-plume inhomogeneities, using both the Daub 11 and median filters. We tested the algorithm in the same way as in the case of the irregular beam geometry using four Daubechies filters and type 1 and type 3 thresholding, with results given in Table 2.

Additionally, we performed simulations using all four preferred Daubechies filters and the median filter to reconstruct a "U-shape" phantom in which the objects are quasi-homogeneous with weakly defined boundaries. We present only the results with the Daub 11 filter. As we can see from its reconstruction in Fig. 14(b), the 'edgy' texture of the original "U-shape" phantom, is lost and the reconstruction appears smooth. The general shape of the two original peaks is partially preserved as well as the link between those two peaks. In all cases, using the wavelet transform in the Landweber algorithm requires a small number of iterations, compared with using the median filter.

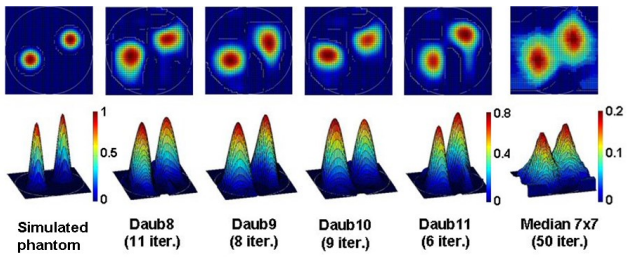

Fig. 13: Image reconstructions obtained from simulated noise-free data using Daub8, Daub9, Daub10 and Daub11 and 7x7 median filter.

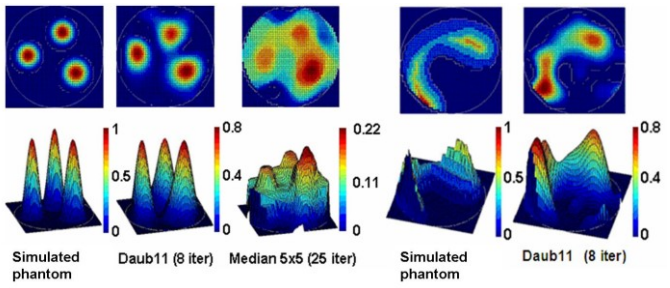

(a) (b)

Fig. 14: Image reconstructions obtained from simulated noise-free data using Daub11, for (a) a triple-plume case, and (b) a "U-shaped" case.

Table 2: Results of reconstructions using different wavelet smoothing and two types of thresholding.

		daub8	daub9	daub10	daub11
fig.13	type1 thr	0.0438	0.4719	0.0467	0.0421
	coef.	0.5	0.5	0.4	0.5
	type3 thr	0.0493	0.0536	0.0485	0.0542
	coef.	0.2	0.2	0.2	0.2
fig14	type1 thr	0.0758	0.0606	0.0701	0.0548
	coef.	0.5	0.8	0.5	0.5
	type3 thr	0.0775	0.0778	0.0752	0.0749
	coef.	0.4	0.3	0.3	0.3
fig.15	type1 thr	0.4156	0.4723	0.4578	0.4508
	coef.	0.5	0.4	0.5	0.5
	type3 thr	0.4766	0.4837	0.4797	0.4558
	coef.	0.2	0.2	0.2	0.2

We conclude again that all the images produced using the Daubechies filters provide better plume separation than the median filter, and that there is some variation in image quality depending on the particular Daubechies filter applied. Table 2 also shows that better results are obtained with type 1 thesholding.

IV. Discussion

The Landweber technique is widely used in practical applications of process tomography, including optical modalities, giving strong motivation for the comparisons presented above. From sections IIB and III above, it is clear that incorporation of a 2D wavelet filter into the Landweber technique requires great care in terms of selecting the optimal mother wavelet function and choosing the appropriate type of thresholding for the wavelet approximation coefficients. In many applications of process tomography, the extent of separation of features within the reconstructed images is crucial. In this respect, it is clear from the results in section III above that the use of the 2D wavelet filter in the Landweber technique offers substantial improvements over median-filter approaches. Any study of the spatial resolution properties of sparse measurement arrays (whether regular or irregular in geometry) is clearly dependent on the filtering technique used. In high-speed applications, such as that in [3], wavelet filtering offers considerable computational advantages compared with median filtering, due to the much-reduced number of iterations required. It is of great interest to consider the use of wavelet filtering for reconstruction of X- and gamma-ray CT in applications with a few hundred measurements per frame. Similarly, its application to so-called soft-field electrical tomography is attractive, since the number of measurements in those cases is typically below 100. In all cases, use of the wavelet technique will help to enhance sensor array design.

V. Conclusions

This paper has presented a novel 2D wavelet-based image reconstruction method that is well suited for very sparse hard-field tomography systems arising from limited sensor access. Wavelet smoothing as a part of the Landweber iteration process shows excellent performance in providing the spatial localization and quantitative imaging of various simulated and experimental phantoms. For both regular and irregular sensor array with severely limited data, various Daubechies wavelet filters show slight differences in performance, as quantified by the average image error per pixel. The computation time of the iterative algorithm with the wavelet filter is significantly improved by reducing the number of iterations, in comparison with median filtering.

VI. References

[1] P. Munshi, "Picking the right solution from a set of correct solutions", Meas. Sci. Technol. 13 (2002) 647–653

[2] P. Wright *et al*., "Toward in-cylinder absorption tomography in a production engine" *Appl. Opt.,* 44(31) 6578-6592, 2005

[3] P. Wright *et al*., "High-speed Chemical Species Tomography in a multi-cylinder automotive engine", *Chem. Eng. J*., doi:10.1016/j.cej.2008.10.026, 2008

[4] A. H. Anderson, "Algebraic reconstruction in CT from limited views", *IEEE Trans. Med. Imaging* 8(1) 50-55, 1989

[5] P. Subbarao *et al.*, "Performance of iterative tomographic algorithms applied to non-destructive evaluation with limited data" *NDT&E International* 30(6), 359-370, 1997

[6] J. Feng and S. L. Bao, "Reconstruction of smooth distribution within unsmooth circumferences from limited views using filtered backprojection algorithm", *Int. J. Imaging Systems Technol.* 12(3) 93-96, 2002

[7] H. Stark *et al.,* "Direct Fourier reconstruction in computer tomography", *IEEE Trans. Acoust. Speech, Signal Processing* 29(2) 237-245, 1981

[8] A. C. Drescher *et al.,* "Novel approach for tomographic reconstruction of gas concentration distributions in air: use of smooth basis functions and simulated annealing", *Atmosph. Environment* 30(6) 929-940, 1996

[9] Z. Feng *et al*., "Design and Implementation of a Self-Validating Pressure Sensor**",** *IEEE Sensors Journal,* 9(3), 207 – 218, 2009

[10] X. Yin *et al*., "2-D Wavelet Segmentation in 3-D T-Ray Tomography", *IEEE Sensors Journal,* 7(3), 342-346, 2007
[11] F. Rashid-Farrokhi *et al.,* "Wavelet-Based Multiresolution Local Tomography," *IEEE Transactions on Image Processing*, vol. 6, No. 10, Oct. 1997, pp. 1412-1430.
[12] T. Olson *et al*., "Wavelet Localization of the Radon Transform," *IEEE Transactions on Signal Processing*, vol. 42, No. 8, Aug. 1994, pp. 2055-2067.
[13] Warrick, *et al*., "A Wavelet Localized Radon Transform", *Proceedings of the SPIE--The International Society for Optical Engineering*, Vol. 2569, Part 2, pp. 632 643, 1995;
[14] Sahiner, *et al.,* "On the Use of Wavelets in Inverting the Radon Transform", *Nuclear Science Symposium and Medical Imaging Conference*, 1992, *IEEE*, Vol. 2, pp. 1129 1131, 25 31 Oct. 1992;
[15] E. Yagle, "Region-of-Interest Tomography Using the Wavelet Transform and Angular Harmonics", *Image Processing, Proceedings*, Vol 2, pp. 461 463, 23 26 Oct. 1995
[16] Srinivasa, *et al*., "Detection of Edges from Projections", *IEEE Trans. on Medical Imaging,* Vol. 11, Issue 1, pp. 76 80, March 1992;
[17] Warrick, *et al*., "Detection of Linear Features Using a Localized Radon Transform with a Wavelet Filter", *Acoustics, Speech, and Signal Processing, 1997, ICASSP-97., 1997 IEEE International Conference*, Vol. 4, pp. 2769 2772, 21 24 Apr. 1997;
[18] D. L. Donoho, "Nonlinear Solution of Linear Inverse Problems by Wavelet-Vaguelette Decomposition", *Applied and Computational Harmonic Analysis*, Vol. 2, Issue 2, pp. 101 126, April 1995;
[19] E. D. Kolaczyk, "Wavelet Shrinkage in Tomography", *Engineering in Medicine and Biology Society, Proceedings of the 16th Annual Inernational Confrerence of the IEEE*, Vol. 2, pp. 1206 1207, 1994;
[20] Lee *et al*., "Wavelet Methods for Inverting the Radon Transform with Noisy Data", *IEEE Transactions on Image Processing*, Vol. 10, Issue 1, pp. 79 94, January 2001;
[21] A. H. Delaney and Y. Bresler, "Multiresolution tomographic reconstruction using wavelets", *IEEE Transactions on Image Processing,* 4 (6), 1995, pp. 799-813
[22] Blanc-Feraud, L. *et al*. "A Fast Tomographic Reconstruction Algorithm in the 2-d Wavelet Transformation Domain", *Int. Conference on Acoustics, Speech, and Signal Processing*, vol. V, Apr. 19-22, 1994, pp. v305-v308.
[23] B. Sahiner and A. E. Yagle, "Limited Angle Tomography using the Wavelet Transform", *IEEE Medical Imaging Conference*, San Francisco, Nov. 4-6, pp. Vol. 3, 1993, pp. 1912-1916
[24] M. Rantala *et al.,* "Wavelet-based reconstruction for limited-angle X-ray tomography", *IEEE Trans. Med. Imaging* 25(2): 210-217, 2006
[25] N. Terzija *et al.,* "Image optimisation for chemical species tomography with an irregular and sparse beam array", *Meas. Sci. Technol.,* 19, 094007, 2008
[26] J. Kovacevic and I. Daubechies (ed), Special Issue on Wavelets, *Proc. IEEE*, vol. 84(4), 1996
[27] S. Mallat, "A Theory for Multiresolution Signal Decomposition: The Wavelet Representation," IEEE Transactions on Pattern Analysis and Machine Intellgence, vol. II, No. 7, Jul. 1989, pp. 674-693.
[28] I. Daubechies, "Orthonormal Bases of Compactly Supported Wavelets", *Comm. Pure and Appl. Math*, Vol. 41, 1988, pp. 909-996
[29] W.Q. Yang *et al.,* "An image-reconstruction algorithms based on Landweber's iteration method for electrical-capacitance tomography", *Meas. Sci. Technol*. 10 1065-9, 1999

VII. APPENDIX

Matlab code for the wavelet smoothing function is given below:

```
function sol_sq=wavelet_smooth(sol_sq, filter, coef, type_thr);
%-----------------------------------------------------

%  input arguments:
% - filter -> Chosen Wavelet filter
% - coef -> percentage of the coefficients needed for threshold calculation
% - type_thr -> selected type of the thesholding,
% type_1- based on setting the coefficients to zero
% which are smaller then the threshold, type_2 ->
% hard thresholding and type_3 % soft thresholding
%-----------------------------------------------------

 %perform DWT
[C,S] = wavedec2(sol_sq,3,filter);
%select the third level of approximation
cA3 = appcoef2(C,S,filter,3);
% find the maximum of cA3
m1=max(max(cA3));
%calculate the threshold
   thr=coef*m1;
 %perform the thresholding
   switch type_thr
       case 'type_1'
         cA3(cA3<thr) =0;
       case 'type_2'
         cA3 = wthresh(cA3,'h',thr);
       case 'type_3'
         cA3 = wthresh(cA3,'s',thr);
   end;
 %set details to zero
  Cn=zeros(size(C));
  Cn(1:S(1,1)*S(1,2))=reshape(cA3,1,S(1,1)*S(1,2));
 %apply IDWT only to the approximations
 sol_sq = waverec2(Cn,S,filter);
```

Nataša Terzija (M'2000) was born in Belgrade, Serbia. She is a Postdoctoral Research Associate in the School of Electrical and Electronic Engineering, The University of Manchester, where she has been since 2007. From 2001 to 2006, she was a Research and Teaching Assistant at the University of Duisburg-Essen, Germany. In 2006 she obtained her PhD at the same University. Her main research interests are image and signal processing, industrial process tomography and data hiding.

Hugh McCann FREng (SM'2003) was appointed Professor of Industrial Tomography in Manchester in 1996, following 10 years in R&D at the Royal Dutch/Shell Group. Educated at the University of Glasgow (BSc 1976, PhD 1980), he worked in High Energy Particle Physics for 10 years at Glasgow, Manchester, CERN (Geneva) and DESY (Hamburg). Professor McCann has extended industrial tomography to provide specific chemical contrast using high-speed all-opto-electronic techniques, and has developed electrical impedance tomography for medical applications, collaborating intensively with users in both academia and industry. He was Head of the School of Electrical & Electronic Engineering (1999-2002), then chaired the UK *Professors & Heads of Electrical Engineering* (2003-2005) and the *Virtual Centre for Industrial Process Tomography* (2005-2009). He was elected a Fellow of the Royal Academy of Engineering in 2009.